IEEE Photonics Journal
An IEEE Photonics Society Publication

Instabilities in Spin-Polarized Vertical-Cavity Surface-Emitting Lasers

Volume 3, Number 5, October 2011

Rihab Al-Seyab
Dimitris Alexandropoulos
Ian D. Henning
Michael J. Adams

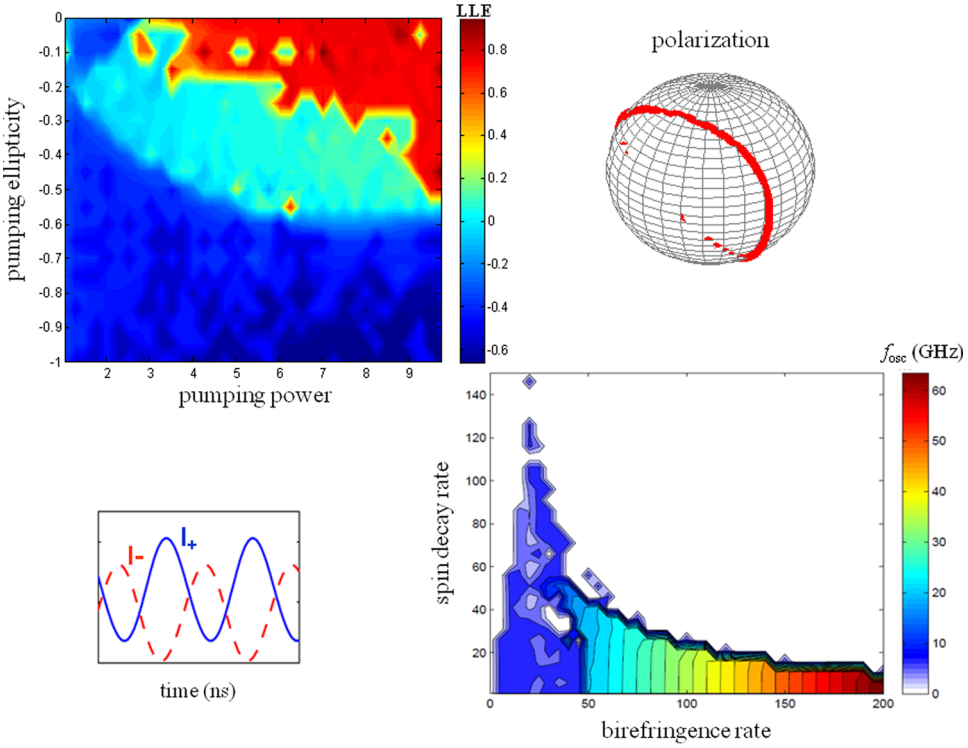

DOI: 10.1109/JPHOT.2011.2165205
1943-0655/$26.00 ©2011 IEEE

IEEE photonics SOCIETY
IEEE

Instabilities in Spin-Polarized Vertical-Cavity Surface-Emitting Lasers

Rihab Al-Seyab,[1] Dimitris Alexandropoulos,[1,2] Ian D. Henning,[1] and Michael J. Adams[1]

[1]School of Computer Science and Electronic Engineering, University of Essex, CO4 3SQ Colchester, U.K.
[2]Department of Materials Science, University of Patras, 26504 Patras, Greece

DOI: 10.1109/JPHOT.2011.2165205
1943-0655/$26.00 ©2011 IEEE

Manuscript received July 21, 2011; revised August 6, 2011; accepted August 9, 2011. Date of publication August 22, 2011; date of current version September 9, 2011. This work was supported by the U.K. Engineering and Physical Sciences Research Council under Grant EP/G012458/1 and Grant EP/H00873X/1. Corresponding author: R. Al-Seyab (e-mail: rksals@essex.ac.uk).

Abstract: We report a first comprehensive theoretical analysis of optically pumped spin-polarized vertical-cavity surface-emitting lasers, which combines the spin-flip model with the largest Lyapunov exponent technique to determine regions of stability and instability. The dependence of these regions on a wide range of fundamental device parameters is investigated, and results were presented in a new form of maps of the polarization versus the magnitude of the optical pump. We also reveal the importance of considering both the birefringence rate and the linewidth enhancement factor when engineering a device for high-frequency applications.

Index Terms: Largest Lyapunov exponent (LLE), optical pumping, spin-flip model, spin-polarized vertical-cavity surface-emitting lasers (VCSELs).

1. Introduction

Spin-polarized vertical-cavity surface-emitting lasers (VCSELs) offer the exciting prospect of output polarization control through the injection of spin-polarized electrons. Such capabilities could lead to many new applications in the field of spectroscopy, communications and information processing. In practice a spin-polarized electron population can be achieved via either electrical injection using magnetic contacts or by optical pumping using circularly polarized light [1], [2]. Recent research advances in this area have included demonstrations of an electrically injected quantum dot spin-VCSEL operating at 200 K [3] and an optically pumped spin-VCSEL grown on a (110) substrate which achieved a high degree of circular polarization associated with an enhanced spin lifetime [4]. A spin relaxation time of 0.7 ns at room temperature was reported in the latter work [5]. However, the ultimate challenge remains to achieve an electrically injected spin-VCSEL with enhanced spin lifetime operating at room temperature.

Complementary theoretical work to model spin-VCSEL behavior is commonly based on the spin-flip model (SFM) [6]–[8]. This represents the carrier populations in the conduction and valence bands in terms of two distinct carrier densities associated with spin-up and spin-down. These are associated with two lasing transitions giving rise to right- or left-handed circularly polarized emission. The two transitions are coupled via the "spin flip" processes which is characterized by a spin relaxation rate (γ_s) between spin up and spin down electrons. The SFM also takes account of the gain anisotropy or dichroism (γ_a) and birefringence (γ_p) rates, which together act to couple orthogonally polarized modes of the VCSEL. The model has shown good agreement with experimental

results for pulsed and continuous optical pumping of spin-VCSELs [9], [10]. In a simplified version of the SFM using rate equations, where the effects of gain anisotropy and birefringence were neglected, performance improvements including threshold reduction were predicted [11], [12]. In a further variation, transitions from the barrier into the quantum well (QW) were incorporated to model optically pumped VCSELs [13], [14] and, with appropriate modification of the pumping term, VCSELs with electrical spin injection [1], [15], [16]. This model has also been used to simulate quantum dot spin-VCSELs by including transitions from the wetting layer to the dot levels while still retaining the simplification of neglecting gain anisotropy and birefringence [15]–[17]. In another approach, it was assumed that the two circularly polarized field components have the same frequency and maintain a constant phase difference [18]. By further assuming that the laser operated in the steady state, this resulted in a computationally efficient solution of the resulting simplified SFM equations. While this allowed an investigation of device properties as a function of a few basic device parameters [19], it only revealed solutions where the laser output was stable and would not therefore reveal regions of chaos or oscillatory behavior, for example.

In contrast to these previous reports, here we use the full SFM equations to present a first systematic and detailed study of spin-VCSEL dynamics over an extensive range of device parameters including spin relaxation, birefringence, electron and photon lifetimes, linewidth enhancement factor, and the magnitude and ellipticity of the pumping. In a further enhancement, the numerical solution of the SFM has been combined with the largest Lyapunov exponent (LLE) method for analysis of the stability of spin-VCSELs. The present paper is a fuller exposition of the work presented in [20] as a preliminary report. We begin by showing examples of the temporal optical output from the spin-VCSEL model which illustrate various forms of behavior ranging from stable emission through to chaotic dynamics and using the Poincare sphere to present these results. We next show results in the form of new detailed stability maps in the plane of polarization versus magnitude of the pumping, where we identify regions of stability and instability which have been systematically computed over a wide range of device parameters. Where possible, we seek comparisons with previous reports in the literature and demonstrate excellent agreement. Finally, we use the model to investigate the high-frequency behavior of period one oscillations. We reveal the importance of considering both the birefringence rate and the linewidth enhancement factor to realize both high oscillation frequency together with good modulation depth.

2. Theory

The SFM equations are conventionally written in terms of the right- and left-circularly polarized complex fields, denoted, respectively, by $\bar{E}_+$ and $\bar{E}_-$, and two populations of electrons: those with spin-down and with spin-up, with corresponding normalized densities n_+ and n_-, respectively. According to the SFM [6]–[8], recombination of spin-down and spin-up electrons in a QW VCSEL produces two lasing transitions for right- and left-circularly polarized electric fields. The spin relaxation process for electrons is characterized by a decay rate γ_s, but spin relaxation of holes in the valence band is assumed to be instantaneous. The SFM rate equations are conventionally expressed in terms of normalized carrier variables $N = (n_+ + n_-)/2$ and $m = (n_+ - n_-)/2$. In addition, circularly polarized pump components (η_+, η_-) can be included to allow for polarized optical pumping. In the case of pumping by electrical current with spin-injecting contacts, the pump terms in the SFM equations can be cast in a similar form [1]. Writing the complex fields in terms of real and imaginary parts as $\overline{E}_\pm = E_{\pm,R} + iE_{\pm,I}$, the rate equations become

$$\frac{dE_{\pm,R}}{dt} = \kappa(N \pm m - 1)(E_{\pm,R} - \alpha E_{\pm,I}) - \gamma_a E_{\pm,R} + \gamma_p E_{\mp,I} \tag{1}$$

$$\frac{dE_{\pm,I}}{dt} = \kappa(N \pm m - 1)(E_{\pm,I} + \alpha E_{\pm,R}) - \gamma_a E_{\pm,I} - \gamma_p E_{\mp,R} \tag{2}$$

$$\frac{dN}{dt} = \gamma\left[\eta_+ + \eta_- - \left(1 + |\overline{E}_+|^2 + |\overline{E}_-|^2\right)N - \left(|\overline{E}_+|^2 - |\overline{E}_-|^2\right)m\right] \tag{3}$$

$$\frac{dm}{dt} = \gamma(\eta_+ - \eta_-) - \left[\gamma_s + \gamma\left(|\overline{E}_+|^2 + |\overline{E}_-|^2\right)\right]m - \gamma\left(|\overline{E}_+|^2 - |\overline{E}_-|^2\right) \tag{4}$$

where $2\kappa = \tau_p^{-1}$ and $\gamma = \tau_n^{-1}$, with τ_p and τ_n as the photon and electron lifetimes, respectively, α is the linewidth enhancement factor and the other symbols are defined in Section 1. We define the total normalized pump $\eta = \eta_+ + \eta_-$ and the pump ellipticity [8]

$$P = \frac{\eta_+ - \eta_-}{\eta_+ + \eta_-}. \tag{5}$$

The ellipticity of the output is given by

$$\varepsilon = \frac{|\overline{E}_+|^2 - |\overline{E}_-|^2}{|\overline{E}_+|^2 + |\overline{E}_-|^2}. \tag{6}$$

Using the full set of equations (1)–(4), which are solved numerically, reveals that there are regions of parameter space where the solutions are unstable and oscillatory behavior is found [8]. In the present study this behavior is found to be associated with birefringence oscillations that are naturally damped by dichroism. That is, the source of these oscillations lies in the competition between fundamental physical processes at work in the device: the spin-flip processes that tend to equalize the gain for right- and left-circularly polarized fields, dichroism which tries to equalize the field amplitudes, and birefringence which couples power back and forth between the polarized fields. Gahl *et al.* [8] have used the SFM to study these and other oscillations present in optically pumped VCSELs, namely Larmor oscillations, which are damped by spin flip, and relaxation oscillations, which are naturally damped by carrier recombination. These various forms of oscillatory behavior can be destabilized by different excitation processes and thus lead to self-sustained oscillations in the polarization of the emitted light even for VCSELs with cw pumping. The regions of oscillatory behavior and those of phase-locked stability are determined by the key control parameters η and P.

This motivates our analysis of the stability of the solutions of the SFM equations; for this purpose we use LLE method which has previously been successfully applied to stability analysis of optically injected lasers [21]. To the best of our knowledge this is the first such analysis of the stability of spin-VCSELs as a function of pumping magnitude η and polarization P. For the case of linearly polarized pumping (equivalent to conventional electrically injected VCSELs), conditions for stability of the linearly polarized modes have been derived by Martin-Regalado *et al.* [7]. For a given value of pumping in the special case where $\gamma_a = 0$, these conditions may be written in terms of critical values of the pumping

$$\eta_x = 1 + \frac{\frac{\gamma_s}{\gamma}}{\alpha\frac{\kappa}{\gamma_p} - 1} \tag{7}$$

$$\eta_y = 1 - \frac{\gamma_s}{\gamma} + 2\alpha\frac{\gamma_p}{\gamma}. \tag{8}$$

The first of these conditions will be used to check against our LLE calculations in the case of $P = 0$.

3. Results

3.1. Effects of the Pumping Power and Ellipticity on Spin-VCSEL Stability

The sensitivity of spin-VCSEL stability to the control parameters η and P is demonstrated in Figs. 1 and 2, respectively. Fig. 1 shows the time response for two step changes in η at $t = 12$ ns from 1.5 to 2.6, and then from 2.6 to 4 at $t = 20$ ns, where the value of P is fixed at -0.1. The SFM parameter set used here is similar to that given in [19]. While the model used in [19] required only ratios of the rates γ_p/κ and γ_s/γ, the SFM solution used here requires values to be specified for each parameter; we therefore choose the values of $\kappa = 125$ GHz, $\gamma = 1$ GHz and $\gamma_a = 0$, $\gamma_p = 20$ GHz, $\gamma_s = 10$ GHz, and $\alpha = 1$. The stable steady-state response that appears in Fig. 1

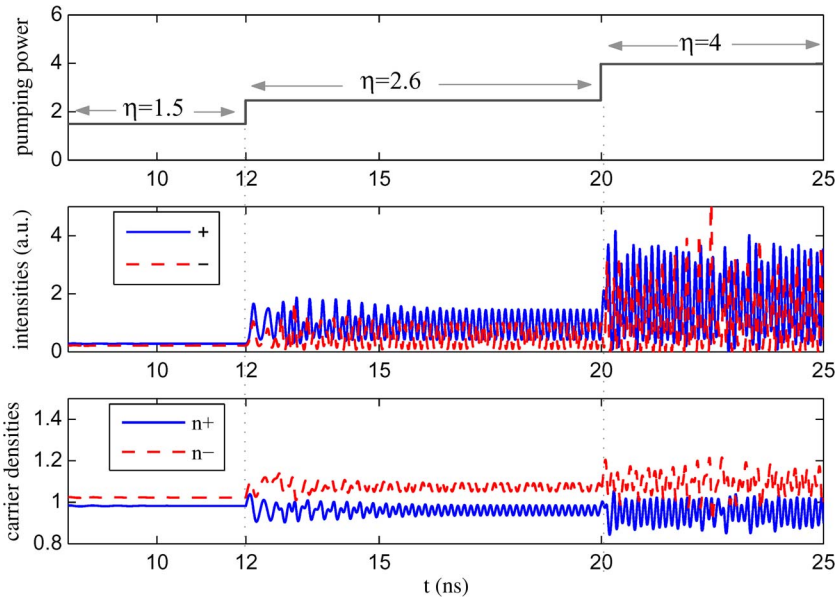

Fig. 1. Calculated time traces for the two circularly polarized intensities and spin-up and spin-down carrier densities using step changes in η from 1.5 to 2.6 at $t = 12$ ns and from 2.6 to 4 at $t = 20$ ns. The value of P is fixed at 0.1. The SFM parameters used here are $\gamma_p = 20$ GHz, $\kappa = 125$ GHz, $\gamma_s = 10$ GHz, $\gamma = 1$ GHz, $\gamma_a = 0$, and $\alpha = 1$ (as reported in [19]).

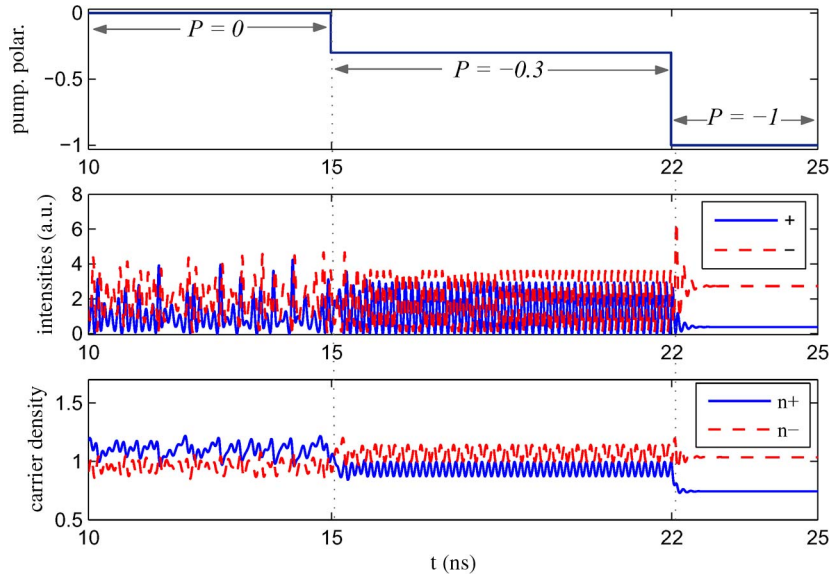

Fig. 2. Calculated time traces for the two circularly polarized intensities and spin-up (spin-down) carrier densities using step changes in P from 0 to -0.3 at $t = 15$ ns and from -0.3 to -1 at $t = 22$ ns. The value of η is fixed at 4. The SFM parameters used here are the same as for Fig. 1.

when $\eta = 1.5$ changes to a periodic oscillation (limit cycle) due to increase of η to 2.6 and then to chaotic oscillation when η is increased to 4.

Similarly, Fig. 2 shows the time response for two step changes in P from linear $(= 0)$ to elliptical $(= -0.3)$ at $t = 15$ ns and then from elliptical to left-circular $(= -1)$ at $t = 22$ ns using a fixed value of $\eta = 4$. The same set of SFM parameters of Fig. 1 is used in Fig. 2. In this case, the response starts with chaotic oscillation at $P = 0$, then changes to periodic (period 1) at $P = -0.3$, and then changes to stable when $P = -1$.

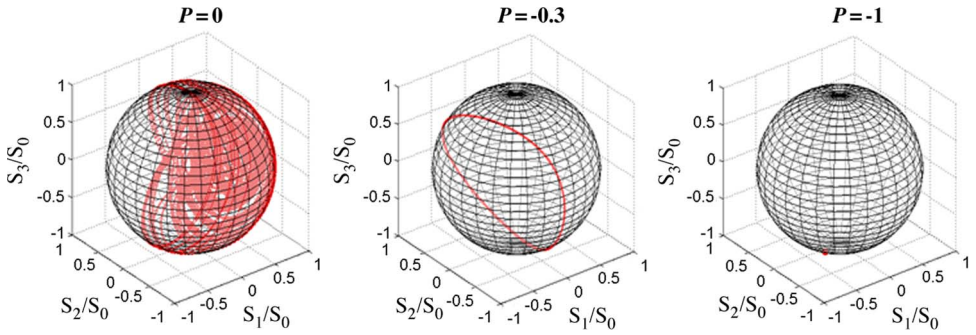

Fig. 3. Poincare sphere and Stokes coordinate system, showing the fluctuation in the output polarization using three different values of the pumping ellipticity: $P = 0$, -0.3, and -1 (see Fig. 2 for comparison). The SFM parameters used here are the same as those in Fig. 1.

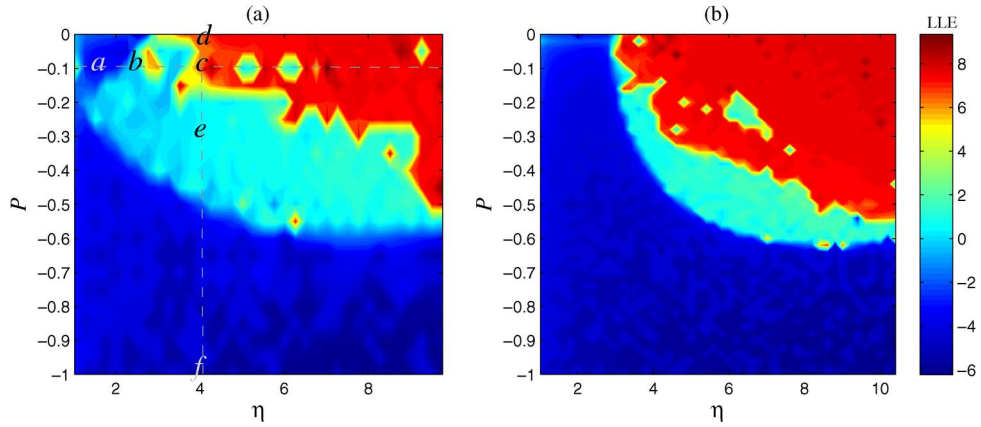

Fig. 4. Stability map calculated for the cases: (a) $\gamma_p = 20$ GHz, $\kappa = 125$ GHz, $\gamma_s = 10$ GHz, $\gamma = 1$ GHz, $\gamma_a = 0$, and $\alpha = 1$ [19]. The letters *a*, *b*, *c* represent the three operating points of Fig. 1, while *d*, *e*, *f* correspond to the three operating points of Fig. 2. (b) $\gamma_p = 11\pi$ GHz, $\kappa = 300$ GHz, $\gamma_s = 40$ GHz, $\gamma = 1.5$ GHz, $\gamma_a = 1.6\pi$ GHz, and $\alpha = 2$ (device parameters as in [23]).

Similar oscillatory behavior has been observed in the output polarization ε, due to varying the pumping power and ellipticity. Fig. 3 uses the Poincare sphere to show the fluctuation in the output polarization ε due to changing the pumping ellipticity. The Stokes parameters S_0, S_1, S_2, and S_3 constitute the Cartesian coordinates of the polarization state, which is represented by a point on the surface of the sphere. Three different cases are observed in Fig. 3, namely i) chaotic behavior where the output polarization oscillates and covers most of the sphere when $P = 0$, ii) periodic oscillation in a limit cycle when P is elliptical $(= -0.3)$, and iii) stability when $P = -1$ or left circular (which appears as a single point near the bottom pole of the sphere).

3.2. Stability Map Calculations Using LLE

To see the whole picture of the dynamic behavior of spin-VCSELs, stability maps in the plane of $\eta - P$ are calculated by combined the numerical solution of the rate equations (1)–(4) with the LLE method. Fig. 4(a) shows a calculated stability map for spin-VCSELs using the same parameter set as in Fig. 1. Since the results are symmetric about $P = 0$, only negative values of P are shown. The color scale is used to define the contours of LLE values with a discrimination in LLE; negative values correspond to stability, zero to oscillatory behavior, and positive values to regions of more complex dynamics tending toward chaos as the LLE increases. For this set of parameters, equation (7) yields $\eta_x = 2.905$, which is clearly close to the value of η seen at $P = 0$ for the limit of stability in

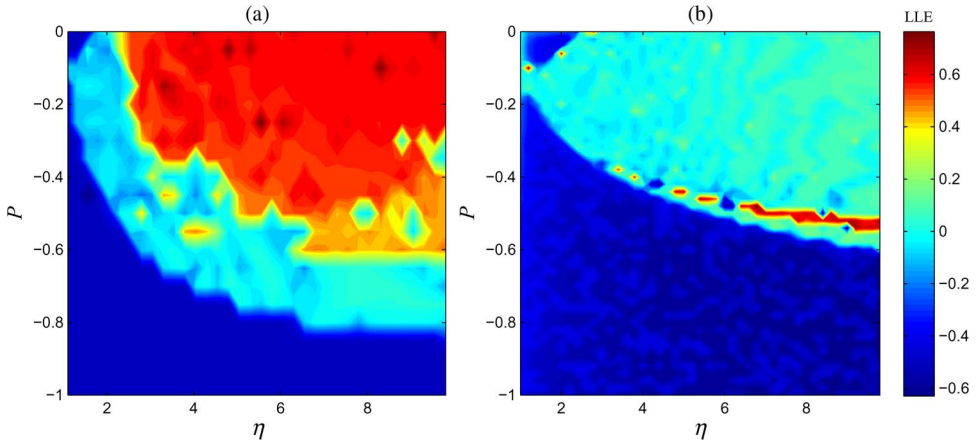

Fig. 5. Calculated stability maps for the case (a) $\gamma_p = 20$ GHz and (b) $\gamma_p = 100$ GHz. In all cases, $\gamma_s = 10$ GHz, $\alpha = 3$, $\gamma = 1$ GHz, $\kappa = 125$ GHz, and $\gamma_a = 0$ (device parameters as in [19]).

Fig. 4(a). It is also interesting to note the fine structure shown within the broad regions defined in Fig. 4(a). This suggests that in practice mixed dynamics might be observed which might be a very sensitive function of operating conditions and could be difficult to define unambiguously. Note that the letters *a*, *b*, *c* on the map refer to the three operating points of Fig. 1 when $\eta = 1.5, 2.6,$ and 4, using a fixed value of $P = -0.1$. Similarly, the letters *d*, *e*, *f* refer to the three operating points of Fig. 2 when $P = 0, -0.3,$ and -1, and using a fixed value of $\eta = 4$.

Experimental results of ultrafast circular polarization oscillations with a frequency of 11 GHz have been reported for electrically–pumped VCSELs with additional spin injection using circularly polarized optical pumping [22], [23]. The authors of [23] have also used the SFM to simulate experimental measurements of picosecond spin dynamics in response to a short-pulse of spin-polarized excitation, using the parameter values $\gamma_p = 11$ GHz, $\kappa = 300$ GHz, $\gamma_s = 40$ GHz, $\gamma = 1.5$ GHz, $\gamma_a = 1.6\pi$ GHz, and $\alpha = 2$. We have used these values to calculate the stability map shown in Fig. 4(b) which is characterized by a large region of instability that grows with increasing pump level. This is consistent with the results of [23].

3.3. Effects of SFM Parameters on the Dynamics

Here, the influence of the SFM parameters on the type of nonlinear dynamics has been investigated. Fig. 5 shows the effect of the birefringence rate γ_p on the dynamics of the instability region of spin-VCSELs. The values of SFM parameters used in both subplots of Fig. 5 are $\gamma_s = 10$ GHz, $\alpha = 3$, $\gamma = 1$ GHz, $\kappa = 125$ GHz, and $\gamma_a = 0$. A value of $\gamma_p = 20$ GHz has been used in Fig. 5(a) and $\gamma_p = 100$ GHz has been used in Fig. 5(b).

The nonlinear dynamics in Fig. 5(a) can be divided into two different regions: period one (P1) oscillation (light blue color) and more complex dynamics or chaotic behavior (orange to red colors) with increasing η. Fig. 5(b) shows that the boundaries and shape of the instability region are not affected very much by increasing γ_p to 100 GHz. However, the types of behavior inside this region have changed significantly. Most of the dynamic behavior in Fig. 5(b) becomes type P1 and the chaotic region shrinks to zero or very tiny areas due to increasing γ_p in this case.

Gahl *et al.* [8] reported the effect of γ_s on the oscillation behavior of spin-VCSELs. In [8] the calculated time series and optical spectra for two different operating points of η and P were given. The two values of spin relaxation rate γ_s that were used were 5 GHz and 150 GHz (see [8, Fig. 7]). The other values of SFM parameters were $\gamma_p = 12\pi$ GHz, $\gamma = 1$ GHz, $\gamma_a = 0.01\gamma_p$, $\alpha = 3$, and $\kappa = 250$ GHz. Here, we have selected the same basic SFM parameters as in [8] for study, but we expand the number of operating points to cover the whole $(\eta - P)$ plane to generate the stability map using LLE shown in Fig. 6.

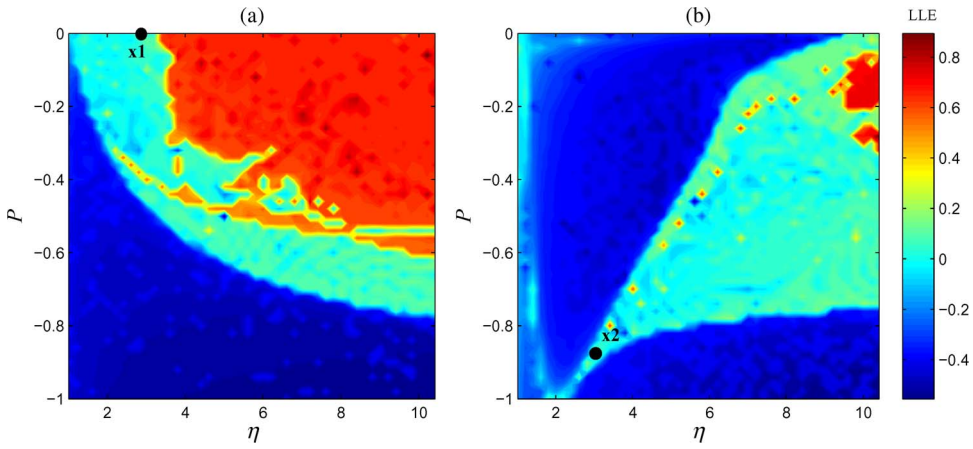

Fig. 6. Calculated stability maps for the case (a) $\gamma_s = 5$ GHz and (b) $\gamma_s = 150$ GHz. In all cases, $\gamma_p = 12\pi$ GHz, $\gamma = 1$ GHz, $\gamma_a = 0.01\gamma_p$, $\alpha = 3$, and $\kappa = 250$ GHz (as given in [8]). The letters x_1 and x_2 refer to the two operating points selected by Gahl *et al.* [8] and using their device parameters.

Fig. 6(a) and (b) show the full stability maps for $\gamma_s = 5$ GHz and 150 GHz, respectively. It is clear that increasing γ_s affects both the shape of the unstable region and the dynamic behavior within it. For example, the high value of γ_s increases the critical pumping power at $P = 0$ to very a large value $= 9.2$ (which is very close to the predicted value using equation (7), $\eta_x = 8.938$). Also, the unstable region changes completely in shape and size. We also see that the effect of increasing γ_s on the type of the oscillation was similar to that of increasing γ_p (i.e., significantly expanding the region of type P1). The points marked x_1 and x_2 in each map of Fig. 6 correspond to the two operating points selected in [8], which showed P1 oscillations. Our results show good agreement with those in [8] also showing P1 behavior. However, from just these two individual points it might be concluded that the device exhibits solely P1 oscillations, whereas from the full maps we present we can clearly see that is not the case. We also investigated the effects of changing the other SFM parameters on the dynamic behavior of spin-VCSELs, generating maps in each case. We find that they have a negligible effect on the unstable region (shape or type of oscillation), and therefore, these results are not included here.

3.4. Frequency of Oscillation

In this section, the effects of the parameters η, P, γ_p, and γ_s on the frequency of the polarization oscillations (type P1) are investigated. Fig. 7 shows a calculated contour map for P1 oscillation frequency (f_{osc}) in the plane $(\eta - P)$ using a fast Fourier transform (FFT) of the time series solutions of equations (1)–(4). The SFM parameters used here are those of the case in Fig. 5(b), where P1 oscillation is present in most of the instability region. Fig. 7 shows that there is no effect of the pumping ellipticity P on the frequency f_{osc}. Increasing the pumping power η from 1 (the normalized threshold value) to 10 increases slightly the value of f_{osc} from 32 GHz to 44 GHz (see the color bar for values in Gigahertz).

To study the effects of γ_p and γ_s on the frequency f_{osc} at one operating point in the plane of $(\eta - P)$, stability maps in the plane of $(\gamma_p - \gamma_s)$ have been calculated. First, Fig. 8(a) shows a calculated stability map using LLE at the operating point $\eta = 5$ and $P = 0$. The other parameters of SFM are those of Fig. 7. In this map the self-sustained polarization oscillations commence when both γ_p and γ_s have very small values; then, the instability region shrinks gradually when γ_p or γ_s increases. Also, the nonlinear dynamics are more chaotic when $\gamma_p \approx 4{-}45$ GHz, and $\gamma_s \approx 0$–130 GHz. The boundaries of the instability region in Fig. 8(a) agree with the calculated boundaries using the stability conditions (7) and (8) when η_x and η_y are set to 5 [see the dashed and dash-dotted lines in Fig. 8(a)].

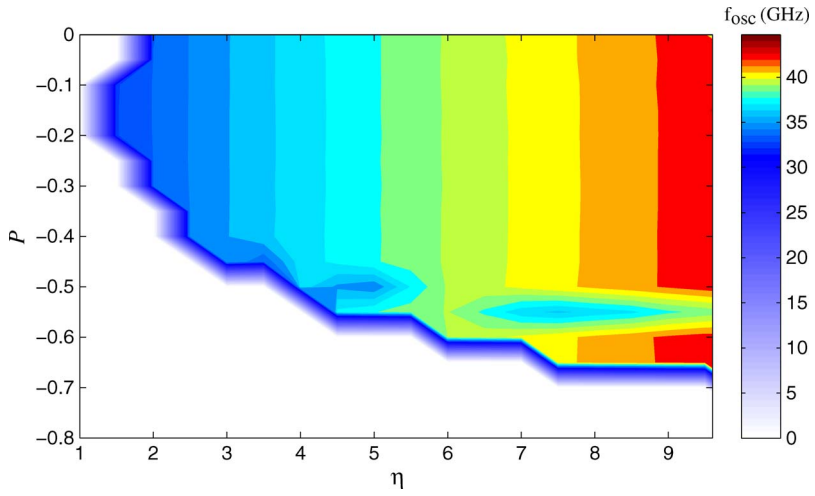

Fig. 7. Calculated contour map of oscillation frequency in the $(\eta - P)$ plane using the parameters of Fig. 5(b). The color bar shows the values of the frequency f_{osc} in Gigahertz.

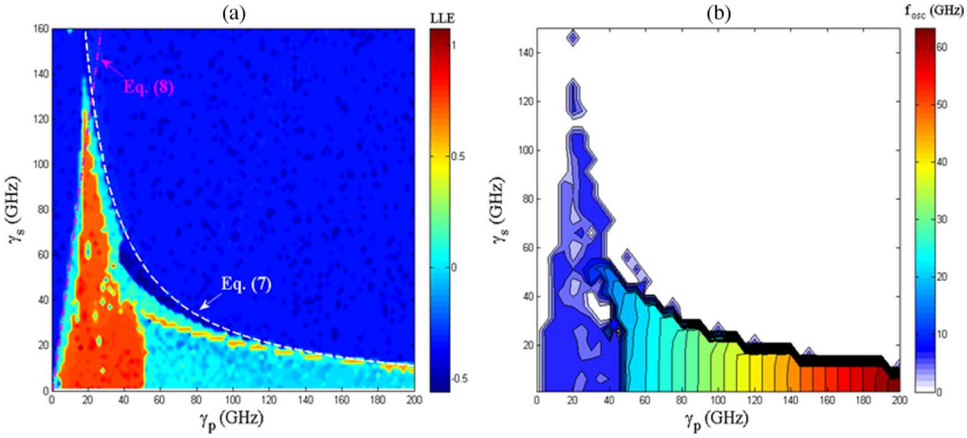

Fig. 8. Calculated stability map using LLE (a) and contour map for the frequency of P1 oscillation (f_{osc}) (b) for the case $\eta = 5$, $P = 0$, $\gamma = 1$ GHz, $\gamma_a = 0$, $\alpha = 3$, and $\kappa = 250$ GHz. The dashed and dash-dotted lines in (a) are calculated using the stability conditions (7) and (8), as given in [7].

Next the effects of γ_p and γ_s on the oscillation frequency of P1 are investigated by calculating a contour map for f_{osc} in the plane $(\gamma_p - \gamma_s)$, as shown in Fig. 8(b). The new map shows clearly that the oscillation frequency can be increased linearly with the birefringence rate, while there is a negligible effect of the spin rate on the frequency. These results agree with the analytic approximation developed by Gahl *et al.* [8]

$$f_b = \frac{1}{2\pi}\sqrt{\gamma_p^2 + \Delta\overline{\omega}_{\pm}^2} \tag{9}$$

where $\Delta\overline{\omega}_{\pm}$ is the average value of, $\Delta\omega_{\pm}$ and $\Delta\omega_{\pm} = 2\kappa\alpha$m. The above equations clearly show that the oscillation frequency f_b is not dependent on γ_s, and depends only on γ_p, κ, and α. Fig. 8(b) shows that increasing γ_p from 60 to 200 GHz can increase the oscillation frequency from approximately 23 GHz to 63 GHz (see the color bar for values in Gigahertz). These values agree with the calculated values using (9) where $f_b = 19.4$ GHz when $\gamma_p = 60$ GHz and $f_b = 63.8$ GHz when

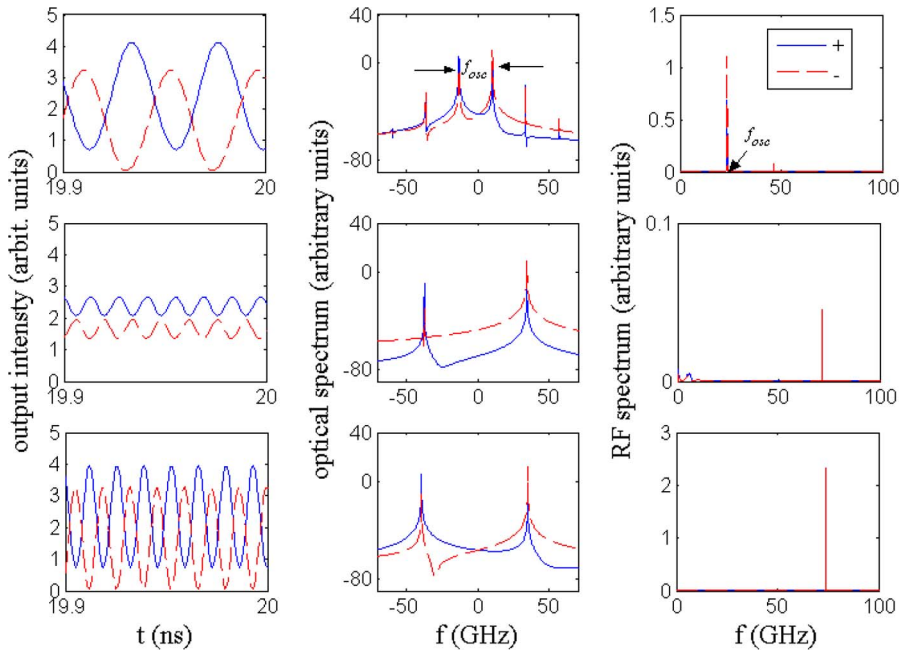

Fig. 9. Calculated time series (left), optical spectra (middle), and RF spectra (right) in the case $\eta = 5$, $P = 0.3$, $\gamma_s = 10$ GHz, $\gamma = 1$ GHz, $\gamma_a = 0$, $\kappa = 250$ GHz, and (a) $\alpha = 3$, $\gamma_p = 60$ GHz; (b) $\alpha = 3$, $\gamma_p = 220$ GHz; and (c) $\alpha = 5$, $\gamma_p = 220$ GHz.

$\gamma_p = 200$ GHz. The importance of the birefringence rate in achieving high-frequency periodic oscillations in spin-VCSELs has also recently been highlighted by Li *et al.* [24].

To demonstrate the effect of γ_p on the oscillation frequency, calculated time series, optical spectra and radio frequency (RF) spectra are given in Fig. 9. Here, $\gamma_p = 60$ GHz, $\alpha = 3$ are used in Fig. 9(a), $\gamma_p = 220$ GHz, $\alpha = 3$ in Fig. 9(b), and $\gamma_p = 220$ GHz, $\alpha = 5$ in Fig. 9(c), respectively. In all cases $\gamma_s = 10$ GHz while $\eta = 5$, $P = 0.3$, and the other SFM parameter values are the same as the case of Fig. 7. Fig. 9(a) and (b) shows that the oscillation frequency, f_{osc} increased from 23.2 GHz when $\gamma_p = 60$ GHz to 71.4 GHz when $\gamma_p = 220$ GHz. However, the new higher frequency was accompanied by a significant reduction in the peak to peak amplitude of the oscillations in both circular polarizations as seen in Fig. 9(b). After further investigations on the effects of the various SFM parameters, it was found that increasing the linewidth enhancement factor from 3 to 5 leads to an enhancement in the amplitude of the oscillations in addition to a small increase in the oscillation frequency of a few Gigahertz. This is well demonstrated in the results of Fig. 9(b) and (c).

Also, increasing α to 5 increased the oscillation frequency from 71.4 GHz to 74 GHz, as shown in the optical and RF spectra in Fig. 9(c).

Fig. 10 summarizes these results and shows very clearly the effect of γ_p and the linewidth enhancement factor on both the oscillation frequency of P1 and the peak-to-peak amplitude of the right circularly polarized oscillatory components (the other parameters used in Fig. 10 are similar to those in Fig. 9). From Fig. 10, we see that when $\alpha = 3$ (solid lines), the frequency f_{osc} increases linearly with γ_p, while the peak-to-peak amplitude of the oscillations is highest for $\gamma_p = 75$ GHz, reducing rapidly for $\gamma_p > \sim 120$ GHz. For this set of parameters, with $\gamma_p = 120$ GHz and $\alpha = 3$, this suggests that the optimum oscillation frequency for high RF power will be around 45 GHz. In contrast, for the case when $\alpha = 5$ (dashed lines), the amplitude of the oscillations shows a weaker dependence on γ_p. Thus, for $\gamma_p = 250$ GHz and $\alpha = 5$, we see that a higher oscillation frequency of $\sim$85 GHz can be reached while at the same time retaining high amplitude oscillations. This is an interesting result when considering engineering such a device as a source of high-frequency optical oscillations, and the results suggests that to get both high-frequency P1 with high RF power the values of both the birefringence and the linewidth enhancement factor should be high.

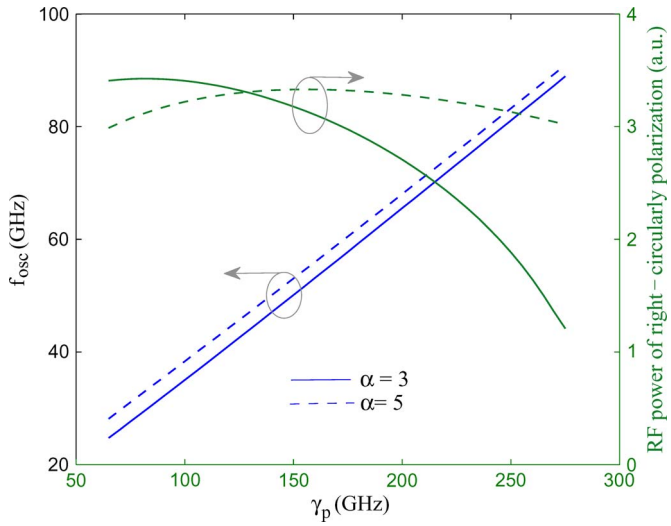

Fig. 10. Oscillation frequency of P1 (left) and the peak-to-peak power (right) plotted against the birefringence rate in the case $\eta = 5$, $P = 0.3$, $\gamma_s = 10$ GHz, $\gamma = 1$ GHz, $\gamma_a = 0$, $\kappa = 250$ GHz, $\alpha = 3$ (solid), and $\alpha = 5$ (dash).

4. Conclusion

In this paper, we present a first systematic and detailed study of spin-VCSEL dynamics over an extensive range of device parameters including spin relaxation, birefringence, electron and photon lifetimes, linewidth enhancement factor, and the magnitude and ellipticity of the pumping. We show examples of the temporal optical output from the spin-VCSEL model and illustrate various forms of behavior ranging from stable emission through to chaotic dynamics. We next present our results in the form of new detailed stability maps in the plane of polarization versus magnitude of the pumping. These results show that there are significant operating regions which, although previously thought to give stable operation, are in fact predicted to have unstable and oscillatory behavior. Where possible, we compare our results with experimental observations of polarization oscillations and picosecond spin dynamics in spin-VCSELs reported by other authors [22], [23] and show good agreement. Finally, we use the model to investigate the high-frequency behavior of period one oscillations. We reveal the importance of considering both the birefringence rate and the linewidth enhancement factor to engineer a device offering both high oscillation frequency and RF power.

Acknowledgment

The authors would like to thank A. Hurtado, K. Schires, and N. Khan at the University of Essex for fruitful discussions.

References

[1] M. Holub and P. K. Bhattacharya, "Spin-polarized light-emitting diodes and lasers," *J. Phys. D, Appl. Phys.*, vol. 40, no. 11, pp. R179–R203, Jun. 2007.
[2] S. Hövel, N. C. Gerhardt, C. Brenner, M. R. Hofmann, F.-Y. Lo, D. Reuter, A. D. Wieck, E. Schuster, and W. Keune, "Spin-controlled LEDs and VCSELs," *Phys. Stat. Sol. (A)*, vol. 204, no. 2, pp. 500–507, Feb. 2007.
[3] D. Basu, D. Saha, C. C. Wu, M. Holub, Z. Mi, and P. Bhattacharya, "Electrically injected InAs/GaAs quantum dot spin laser operating at 200 K," *Appl. Phys. Lett.*, vol. 92, no. 9, p. 091 119, Mar. 2008.
[4] H. Fujino, S. Koh, S. Iba, T. Fujimoto, and H. Kawaguchi, "Circularly polarized lasing in a (110)-oriented quantum well vertical-cavity surface-emitting laser under optical spin injection," *Appl. Phys. Lett.*, vol. 94, no. 13, p. 131108, Mar. 2009.
[5] S. Iba, S. Koh, K. Ikeda, and H. Kawaguchi, "Room temperature circularly polarized lasing in an optically spin injected vertical-cavity surface-emitting laser with (110) GaAs quantum wells," *Appl. Phys. Lett.*, vol. 98, no. 8, p. 081113, Feb. 2011.

[6] M. San Miguel, Q. Feng, and J. V. Moloney, "Light-polarization dynamics in vertical cavity surface-emitting lasers," *Phys. Rev. A*, vol. 52, no. 2, pp. 1728–1739, Aug. 1995.
[7] J. Martin-Regalado, F. Prati, M. San Miguel, and N. B. Abraham, "Polarization properties of vertical-cavity surface emitting lasers," *IEEE J. Quantum Electron.*, vol. 33, no. 5, pp. 765–783, May 1997.
[8] A. Gahl, S. Balle, and M. San Miguel, "Polarization dynamics of optically pumped VCSELs," *IEEE J. Quantum Electron.*, vol. 35, no. 3, pp. 342–351, Mar. 1999.
[9] N. Gerhardt, S. Hovel, M. Hofmann, J. Yang, D. Reuter, and A. Wieck, "Enhancement of spin information with vertical cavity surface emitting lasers," *Electron. Lett.*, vol. 42, no. 2, pp. 88–89, Jan. 2006.
[10] S. Hovel, N. Gerhardt, M. Hofmann, J. Yang, D. Reuter, and A. Wieck, "Spin controlled optically pumped vertical cavity surface emitting laser," *Electron. Lett.*, vol. 41, no. 5, pp. 251–253, Mar. 2005.
[11] C. Gøthgen, R. Oszwaldowski, A. Petrou, and I. Zutic, "Analytical model of spin-polarized semiconductor lasers," *Appl. Phys. Lett.*, vol. 93, no. 4, p. 042513, Jul. 2008.
[12] J. Lee, W. Falls, R. Oszwaldowski, and I. Zutic, "Spin modulation in semiconductor lasers," *Appl. Phys. Lett.*, vol. 97, no. 4, p. 041116, Jul. 2010.
[13] J. Rudolph, D. Hagele, H. M. Gibbs, G. Khitrova, and M. Oestreich, "Laser threshold reduction in a spintronic device," *Appl. Phys. Lett.*, vol. 82, no. 25, pp. 4516–4518, Jun. 2003.
[14] J. Rudolph, S. Dohrmann, D. Hagele, M. Oestreich, and W. Stolz, "Room temperature threshold reduction in vertical cavity surface-emitting lasers by injection of spin-polarized electrons," *Appl. Phys. Lett.*, vol. 87, no. 24, p. 241117, Dec. 2005.
[15] M. Holub, J. Shin, D. Saha, and P. Bhattacharya, "Electrical spin injection and threshold reduction in a semiconductor laser," *Phys. Rev. Lett.*, vol. 98, no. 14, p. 146603, Apr. 2007.
[16] D. Basu, D. Saha, and P. Bhattacharya, "Optical polarization modulation and gain anisotropy in an electrically injected spin laser," *Phys. Rev. Lett.*, vol. 102, no. 9, p. 093 904, Mar. 2009.
[17] R. Ozwaldowski, C. Gothgen, and I. Zutic, "Theory of quantum dot spin-lasers," *Phys. Rev. B*, vol. 82, no. 8, p. 085316, Aug. 2010.
[18] A. Dyson and M. J. Adams, "Spin-polarized properties of optically pumped vertical cavity surface emitting lasers," *J. Opt. B, Quantum Semiclass. Opt.*, vol. 5, no. 3, pp. 222–226, Apr. 2003.
[19] M. J. Adams and D. Alexandropoulos, "Parametric analysis of spin-polarized VCSELs," *IEEE J. Quantum Electron.*, vol. 45, no. 6, pp. 744–749, Jun. 2009.
[20] R. K. Al Seyab, D. Alexandropoulos, I. D. Henning, and M. J. Adams, "Stability analysis of spin-polarized VCSELs," in *CLEO/Europe EQEC Conf. Dig., OSA Tech. Dig.*, Munich, Germany, 2011, Paper CB_P22.
[21] K. E. Chlouverakis and M. J. Adams, "Stability maps of injection locked laser diodes using the largest Lyapunov exponent," *Opt. Commun.*, vol. 216, no. 4, pp. 405–412, Feb. 2003.
[22] N. C. Gerhardt, M. Li, H. Jaehme, H. Soldat, M. R. Hofmann, and T. Ackemann, "Ultrafast circular polarization oscillations in spin-polarized vertical-cavity surface-emitting laser devices," *Proc. SPIE*, vol. 7597, p. 75970Q, Jan. 25–28, 2010.
[23] M. Y. Li, H. Jaehme, H. Soldat, N. C. Gerhardt, M. R. Hofmann, and T. Ackemann, "Birefringence controlled room temperature picoseconds spin dynamics close to the threshold of vertical-cavity surface-emitting laser devices," *Appl. Phys. Lett.*, vol. 97, no. 19, p. 191114, Nov. 2010.
[24] M. Y. Li, H. Jaehme, H. Soldat, N. C. Gerhardt, M. R. Hofmann, and T. Ackemann, "Birefringence and spin controlled ultrafast polarization oscillations in vertical-cavity surface-emitting lasers," in *CLEO/Europe EQEC Conf. Dig., OSA Tech. Dig.*, Munich, Germany, 2011, Paper CB1_3.